

Superoxide Ion Encaged in Nanoporous Crystal $12\text{CaO}\cdot 7\text{Al}_2\text{O}_3$ Studied by Continuous Wave and Pulsed Electron Paramagnetic Resonance

Satoru Matsuishi,[†] Katsuro Hayashi,[‡] Masahiro Hirano,[§] Isao Tanaka,^{||} and Hideo Hosono^{*,†,‡,§}

Materials and Structures Laboratory, Tokyo Institute of Technology, Mailbox R3-1, Nagatsuta, Midori-ku, Yokohama 226-8503, Japan, Frontier Collaborative Research Center, Tokyo Institute of Technology, Mailbox S2-13, Nagatsuta, Midori-ku, Yokohama 226-8503, Japan, ERATO-SORST, Japan Science and Technology, Mailbox S2-13, Nagatsuta, Midori-ku, Yokohama 226-8503, Japan, and Center for Crystal Science and Technology, University of Yamanashi, Miyamae 7, Kofu, Yamanashi 400-8511, Japan

Received: July 9, 2004; In Final Form: September 10, 2004

Continuous wave and pulsed electron paramagnetic resonance studies were performed on the superoxide ion, O_2^- , encaged in the nanoporous crystal $12\text{CaO}\cdot 7\text{Al}_2\text{O}_3$ (C12A7). Hyperfine splitting due to ^{17}O in O_2^- was observed in C12A7 heated in 40% ^{17}O -enriched O_2 gas at 550 °C, providing solid evidence that encaged O_2^- derives from gaseous O_2 in the atmosphere via reactions with free oxygen ions in the cage. Angular variations of g values, ^{17}O hyperfine splitting in the single crystal at 20 K, and ^{27}Al electron spin–echo envelope modulation pattern for the powder at 4 K clarified that an O_2^- is encaged in a subnanometer-sized cage of C12A7 and adsorbed on a Ca^{2+} ion forming a part of the cage wall. Further, two oxygen atoms in the O_2^- ion are equivalent in the cage, indicating that the O_2^- ion takes a “side-on” configuration. Then, the O–O bond is perpendicular to the 2-fold rotation axis ($C_2 \parallel \langle 100 \rangle$) across the center of the cage and directed to two oxygen ions forming the cage wall. Variation in the g values with temperature indicates that the O_2^- may be regarded as solidlike below ~ 20 K and above this temperature the rocking motion of the O–O bond about the C_2 axis is activated with an increase in temperature, but the anisotropy in the motion remains even at 400 K. This result may be explained by a view that Coulombic interaction of the Ca^{2+} with the fully occupied π orbital in the O_2^- is stronger than that with the semioccupied π orbital, controlling the dynamics.

Introduction

Oxygen exists as divalent anion O^{2-} in most oxide crystals. However, there are a few cases where oxygen forms active species with different valences, O^- , O_2^- , and O_3^- .¹ These active oxygen radicals have attracted much attention for their activities in catalytic materials such as oxidation of hydrocarbons. For example, the role of the active oxygen radical for chemical reactions on MgO surfaces has been extensively studied.² However, it is difficult to produce a large amount of the oxygenic radicals and store them stably, especially for O^- with its extremely strong oxidation power.³

In previous papers, we reported the generation of O_2^- and O^- in a $12\text{CaO}\cdot 7\text{Al}_2\text{O}_3$ (C12A7) crystal in a wide concentration range up to $1 \times 10^{21} \text{ cm}^{-3}$.^{4–6} C12A7 is a thermally stable crystal with a melting point of 1415 °C, and a single crystal can be grown directly from a congruent melt.⁷ The crystal structure consists of densely packed subnanometer-sized cages with a positive charge. Figure 1a shows a schematic representation of the C12A7 crystal lattice. The unit cell of C12A7 includes two molecules, and the crystal lattice of C12A7 belongs to a space group $I\bar{4}3d$ (cubic) with a lattice constant $a = 1.199$ nm. The chemical formula for the unit cell may be represented as $[\text{Ca}_{24}\text{Al}_{28}\text{O}_{64}]^{4+} + 2\text{O}^{2-}$ (the former denotes the lattice framework and the latter is called “free oxygen ion”). Each cage

has a free inner space of ~ 0.4 nm in diameter and a mean effective charge of $+1/3$ (+4 charges/12 cages) (see Figure 1b). A free oxygen ion is accommodated in a cage to compensate for the positive charge of the framework and coordinated by six Ca^{2+} ions. This is similar to an O^{2-} in CaO having rock salt structure as illustrated in Figure 1c. In CaO, six Ca^{2+} ions, which occupy crystallographically equivalent sites, form in a regular octahedron with O_h symmetry. However, six Ca^{2+} ions in C12A7 form a distorted octahedron with S_4 symmetry. Then, the separation (0.28–0.32 nm) between Ca^{2+} and free oxygen ion is $\sim 50\%$ longer than that in CaO (0.24 nm), indicating that the free oxygen ion is loosely bound in the cage. The cage has open doorways of ~ 0.1 nm in diameter, and they control mass transport between the inner cage and the outside. This feature provides flexibility for replacing the free oxygen ions with other anions such as F^- , Cl^- , and OH^- .^{8,9}

Recently, we found new types of C12A7 encaging hydride anion H^- or electron in place of the free oxygen ion.¹⁰ H^- with ($1s^2$) electron configuration is one of the most powerful reducing species. In C12A7 encaging H^- (C12A7: H^-), H^- is easily ionized with UV photons to a pair of H^0 and e^- . The resulting electron can hop between neighboring cages.¹¹ As a consequence, C12A7: H^- is converted into a persistent electronic conductor with electrical conductivity up to 10 S cm^{-1} .¹² Next, we succeeded in replacing $\sim 100\%$ of the free oxygen ions with electrons by utilizing reaction with calcium metal, leading to the formation of high density ($\sim 2 \times 10^{21} \text{ cm}^{-3}$) electrons almost localized in the cages with conductivity up to 100 S cm^{-1} .^{13,14} The resultant electron-encaging C12A7 (C12A7: e^-) may be regarded as “electride” in which an electron works as an anion.

* Author to whom correspondence should be addressed. E-mail: hosono@msl.titech.ac.jp.

[†] Materials and Structures Laboratory, Tokyo Institute of Technology.

[‡] Frontier Collaborative Research Center, Tokyo Institute of Technology.

[§] ERATO-SORST, Japan Science and Technology.

^{||} Center for Crystal Science and Technology, University of Yamanashi.

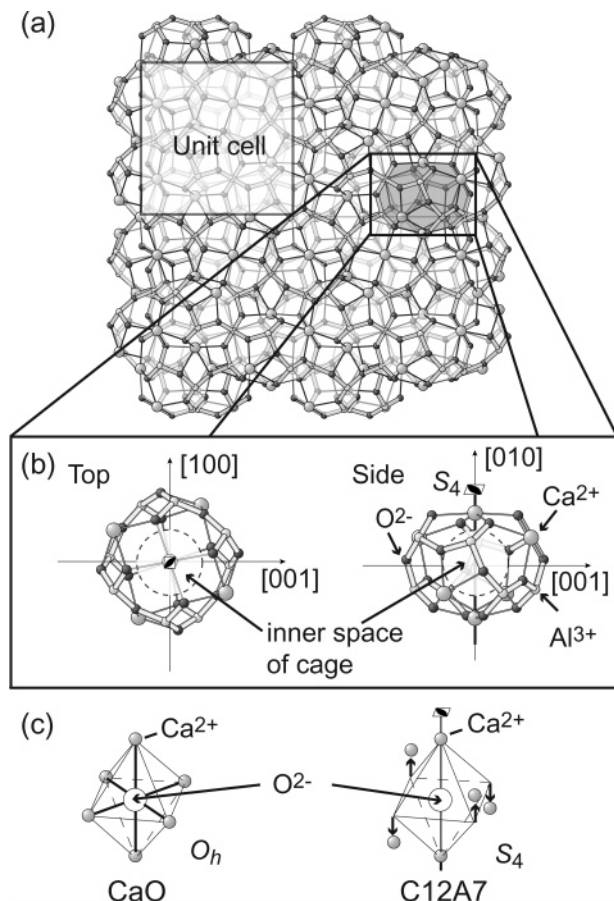


Figure 1. (a) Crystal structure of C12A7. The chemical composition of the unit cell is represented by $[\text{Ca}_{24}\text{Al}_{28}\text{O}_{64}]^{4+}(\text{O}^{2-})_2$. $[\text{Ca}_{24}\text{Al}_{28}\text{O}_{64}]^{4+}$ and $(\text{O}^{2-})_2$ denote a positively charged lattice framework forming 12 cages and “free oxygen” ions encaged in 2 out of 12 cages in the unit cell, respectively. The free oxygen ions are omitted in this figure for simplicity. (b) Top and side views of the cage structure, which is composed of 6 Ca^{2+} , 8 Al^{3+} , and 16 O^{2-} ions. (c) The clathrate oxygen ion in the cage represented by O^{2-} (free oxygen) is coordinated by 6 Ca^{2+} ions, forming a distorted octahedron having S_4 symmetry, whereas O^{2-} in a CaO crystal with rock salt structure is coordinated by 6 Ca^{2+} ions forming a regular octahedron with O_h symmetry.

In the case of C12A7: O^- , a field-assisted monochromic and high-intensity O^- ion beam was achieved.^{15,16} Similarly, C12A7: e^- works as a cold electron emitter with a small work function (~ 0.6 eV), and its application as a display device was demonstrated.¹⁷

As described above, C12A7 provides unique nanometer-sized space surrounded by a positive charge. Such a nanospace may stabilize active anions, including electrons, which are unstable species in a conventional environment. An issue to be clarified is the clathrate state of these anions in the cage.

This paper reports detailed information about the configuration and dynamics of O_2^- encaged in C12A7. Because O_2^- is formed by an addition of an electron to one of the degenerate π_g orbitals of the oxygen molecule O_2 to give the electron configuration $\sigma_g^4\pi_u^4\pi_g^3$ with a $^2\Pi_{3/2}$ ground state ($S = 1/2$), it was identified by the g values obtained from continuous wave electron paramagnetic resonance (CW-EPR) spectra in our previous studies.^{4,5} In the present study, we explored more direct evidence for the presence of O_2^- given by ^{17}O EPR hyperfine structure (HFS). Because of the natural abundance of ^{17}O isotope, having a nuclear spin $I = 5/2$, is very low (0.038%), the EPR spectrum is dominated by the structureless signal due to dominant ^{16}O with $I = 0$ (99.7%). Thus, ^{17}O abundance in

O_2^- was enhanced by heating a C12A7 crystal in ^{17}O -enriched O_2 gas. A C12A7 single crystal was used to observe well-resolved HFS and to analyze angular dependence of ^{17}O hyperfine and g tensors. The analysis reveals the orientation of O_2^- to the crystal axes and configuration to an adsorbing cation at low temperature. This geometrical information suggests the clathrate configuration of O_2^- in the cage of C12A7. EPR superhyperfine structure (SHFS) due to ^{27}Al nuclei ($I = 5/2$, natural abundance 100%) around O_2^- is observed to confirm this structure. However, the splitting is so small that SHFS is hidden in a broad line width of the CW-EPR spectrum. Thus, electron spin-echo envelope modulation (ESEEM) is measured by pulsed EPR, which gives SHFS due to magnetic nuclei in an intermediate range structure around an unpaired electron.^{18–20} Because the ESEEM patterns sensitively reflect the distance and number of ^{27}Al nuclei around O_2^- within the 0.3–0.8 nm in diameter space, we can determine the site of O_2^- in the cage through comparison of an observed pattern with a calculated pattern for the model structure. In addition to these experiments, the temperature variation in the g values was measured in the range 4–400 K to reveal dynamics of O_2^- in the cage.

Experimental Section

Sample Preparation. Polycrystalline C12A7 ceramics were synthesized by solid-state reactions between CaCO_3 and $\gamma\text{-Al}_2\text{O}_3$ for 12 h in an ambient atmosphere at 1350 °C. It contains O_2^- in the concentration of $4 \times 10^{19} \text{ cm}^{-3}$ but does not include detectable O^- . The single crystalline sample, grown by a floating zone method, was cut into a 1-mm-sized cube with (100) surfaces.²¹ The concentration of O_2^- in the as-grown crystal was below 10^{18} cm^{-3} . To enhance the concentration, the crystal was sealed in a silica glass tube filled with 1 atm oxygen gas and heated at 550 °C for 96 h.²² The concentration was increased to $4 \times 10^{19} \text{ cm}^{-3}$ by this treatment. Further, a piece of the crystal was heated in 40% ^{17}O -enriched O_2 gas to enrich ^{17}O in the O_2^- .

CW-EPR Measurements. EPR spectra were measured with a Bruker E580 X-Band (9.6 GHz) EPR spectrometer. In CW-EPR experiments, a TE_{102} mode double rectangular resonator was used. This cavity can be equipped with two types of temperature control systems. One is a cryogenic system using liquid helium as coolant (4–300 K), and the other is a gas flow system using liquid and gaseous nitrogen (100–400 K). Polycrystalline C12A7 was measured to observe powder patterns. For the measurement of angular dependence of the spectra, the single-crystal sample was mounted on the end face of the silica glass rod and inserted into the cavity. The concentration of O_2^- was estimated by the comparison of the EPR area intensity with that of a standard sample $\text{CuSO}_4 \cdot 5\text{H}_2\text{O}$.

Pulsed-EPR Measurements. A split ring resonator inserted into the helium cryostat was used. Polycrystalline C12A7 sealed in a silica glass tube was inserted into the resonator, and a static magnetic field of 340 mT ($g = 2.01$) was applied. In two-pulse experiments, an electron spin of an O_2^- was excited by two microwave pulses called “ $\pi/2$ ” and “ π ” separated by a time interval τ . When the spin-spin relaxation time (T_2) became longer than several hundred ns below ~ 40 K, electron spin-echo (ESE) was observed in a pulse sequence ($\pi/2 - \tau - \pi - \tau - \text{echo}$).²² The intensity of ESE increased with decreasing temperature. With the intensity of ESE being monitored as a function of τ , an exponential decay curve with a time constant T_2 was obtained. In three-pulse experiments, three $\pi/2$ pulses were used, and ESE was observed in the pulse sequence ($\pi/2 - \tau - \pi/2 - T - \pi/2 - \tau - \text{echo}$). With the intensity of ESE being

measured as a function of time interval T with a fixed τ , an echo decay curve with a time constant T_1 , the spin–lattice relaxation time, was obtained.

Periodic modulation having an NMR frequency of ^{27}Al nuclei, called electron spin–echo envelope modulation (ESEEM), was superimposed on a two- or three-pulsed echo decay curve. The amplitude and time-domain variation of ESEEM reflect the number and distance of ^{27}Al around O_2^- . The ESEEM pattern was extracted by dividing an observed decay curve by an exponential decay curve with a time constant T_1 or T_2 . For ESEEM spectral analysis, a three-pulsed echo decay curve measured at 4 K was used.

Simulation of Three-Pulsed ESEEM Pattern. The spin Hamiltonian for the system consisting of an electron spin $S = 1/2$ and a nuclear spin $I > 1$, such as ^{27}Al nuclear ($I = 5/2$), is represented by eq 1

$$\hat{\mathcal{H}}_0 = \hat{\mathcal{H}}_{\text{EZ}} + \hat{\mathcal{H}}_{\text{NZ}} + \hat{\mathcal{H}}_{\text{HF}} + \hat{\mathcal{H}}_{\text{NQ}} \quad (1)$$

The terms on the right-hand side of eq 1 represent electronic-Zeeman (EZ), nuclear-Zeeman (NZ), hyperfine (HF), and nuclear quadrupole (NQ) interactions, respectively. In a system of coordinates rotating around the direction of external magnetic field H_0 with a frequency ν equal to the carrier frequency of the microwave pulses, the Hamiltonian of the system is

$$\tilde{\mathcal{H}}_0 = \hat{\mathcal{H}}_0 - \nu \hat{S}_z \quad (2)$$

where \hat{S}_z is the component of the spin angular momentum parallel to the direction of the external magnetic field.

In the rotating system, eq 1 may be written as

$$\tilde{\mathcal{H}}_0 = \{\nu_0(\theta, \phi) - \nu\} \hat{S}_z + \nu_n \hat{I}_z + \hat{S}_z A \hat{I}_z + \hat{S}_z B \hat{I}_x + \hat{\mathcal{H}}_Q \quad (3)$$

where A and B are HF coupling constants given by

$$A = T_\perp (3 \cos^2 \theta_A - 1) + A_{\text{iso}} \quad (4)$$

$$B = 3T_\perp \sin \theta_A \cos \theta_A \quad (5)$$

$$T_\perp = \frac{g_e \beta_e}{H_0 r^3} \nu_n \quad (6)$$

$$\hat{\mathcal{H}}_Q = \frac{e^2 q Q / h}{4I(2I-1)} \left[\left(1 - \frac{3}{2} \sin^2 \theta_Q \right) (3\hat{I}_z^2 - \hat{I}^2) + \frac{3}{8} \sin^2 \theta_Q (\hat{I}_x^2 - \hat{I}_y^2) \right] \quad (7)$$

Here, the HF and NQ tensors are assumed to be axial, and θ_A and θ_Q denote the angles between the static magnetic field direction and the principal axes of HF and NQ tensors, respectively, r is the distance between unpaired electron and interacting magnetic nucleus, and A_{iso} and $e^2 q Q / h$ denote the isotropic hyperfine interaction and the nuclear quadrupole coupling constant, respectively. The resonance frequency of electron spin ν_0 is a function of the magnetic field direction (θ, ϕ) described by using the g tensor obtained by CW-EPR analysis.

For the case of $S = 1/2$ system, two operators \hat{J}_α and \hat{J}_β describing the spin interactions at α and β components of electron spin are used to calculate ESEEM pattern in place of $\tilde{\mathcal{H}}_0$.

$$\hat{J}_\alpha = \frac{1}{2} \{ \nu_0(\theta, \phi) - \nu \} \hat{I}_e + \nu_n \hat{I}_z + \frac{1}{2} (A \hat{I}_z + B \hat{I}_x) + \hat{\mathcal{H}}_Q \quad (8)$$

$$\hat{J}_\beta = -\frac{1}{2} \{ \nu_0(\theta, \phi) - \nu \} \hat{I}_e + \nu_n \hat{I}_z - \frac{1}{2} (A \hat{I}_z + B \hat{I}_x) + \hat{\mathcal{H}}_Q$$

Here, \hat{I}_e is a $(2I + 1)^2$ unit matrix. Then, the normalized intensity of the three-pulsed echo is obtained by using eq 9 as a function of pulse interval τ and T .^{23,24}

$$V(\tau, T) = \frac{1}{2} [V_\alpha(\tau, T) + V_\beta(\tau, T)] \quad (9)$$

where

$$V_\alpha(\tau, T) = \frac{1}{2I + 1} \text{Re}[\text{Tr}\{e^{-i2\pi\hat{J}_\alpha(\tau+T)} e^{-i2\pi\hat{J}_\beta\tau} e^{i2\pi\hat{J}_\alpha(\tau+T)} e^{i2\pi\hat{J}_\beta\tau}\}] \quad (10)$$

and

$$V_\beta(\tau, T) = \frac{1}{2I + 1} \text{Re}[\text{Tr}\{e^{-i2\pi\hat{J}_\beta(\tau+T)} e^{-i2\pi\hat{J}_\alpha\tau} e^{i2\pi\hat{J}_\beta(\tau+T)} e^{i2\pi\hat{J}_\alpha\tau}\}] \quad (11)$$

The three-pulsed ESEEM pattern induced by N nuclear spins is given by the equation

$$V_N(\tau, T) = \frac{1}{2} \left[\prod_{i=1}^N V_{\alpha,i}(\tau, T) + \prod_{i=1}^N V_{\beta,i}(\tau, T) \right] \quad (12)$$

$$i = 1, 2, \dots, N$$

Here, $V_{\alpha,i}$ and $V_{\beta,i}$ are calculated for i th nucleus by using eqs 10 and 11. For a random system such as powder sample, the modulation pattern can be obtained by averaging over the magnetic field direction (θ, ϕ) to the crystal axis.

$$\langle V_N(\tau, T) \rangle_{\theta, \phi} = \frac{1}{4\pi} \int_0^{2\pi} \int_0^\pi V_N(\tau, T) \sin \theta \, d\theta \, d\phi \quad (13)$$

For the case of C12A7, the direction of the principal axis of Al HF tensor is parallel to the vector \mathbf{r} directed from O_2^- (X_O, Y_O, Z_O) to Al nuclear ($X_{\text{Al}}, Y_{\text{Al}}, Z_{\text{Al}}$), which is given by eq 14.

$$\mathbf{r} = \begin{pmatrix} X_{\text{Al}} - X_O \\ Y_{\text{Al}} - Y_O \\ Z_{\text{Al}} - Z_O \end{pmatrix} \quad (14)$$

Then, $\cos \theta_A$ in eqs 4 and 5 is obtained by the following equation

$$\cos \theta_A = \frac{\mathbf{H} \cdot \mathbf{r}}{|\mathbf{H}| |\mathbf{r}|} \quad (15)$$

where

$$\mathbf{H} = H_0 \begin{pmatrix} \cos \theta \sin \phi \\ \cos \theta \cos \phi \\ \sin \theta \end{pmatrix} \quad (16)$$

In addition to the HF tensor, we set the direction of the principal axis of the NQ tensor. In an axial tensor model, this direction is parallel to that of electric field at the nuclear position. Through a consideration on the crystal structure of C12A7 (Table 4) and the symmetries of the two types of AlO_4 groups in Figure 2, the direction of the electric field $\mathbf{q} = (q_x, q_y, q_z)$ was determined as shown in this figure. The following equation gives $\cos \theta_Q$ in eq 7

$$\cos \theta_Q = \frac{\mathbf{H} \cdot \mathbf{q}}{|\mathbf{H}| |\mathbf{q}|} \quad (17)$$

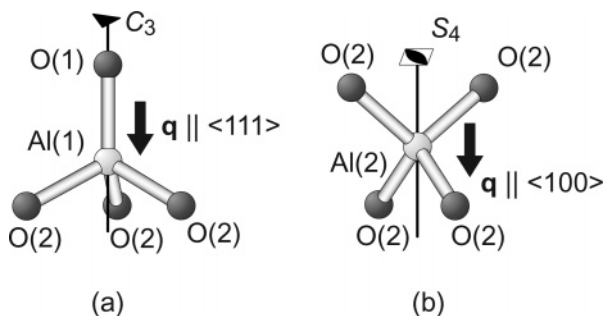


Figure 2. The coordination structure around two types of Al^{3+} ions in C12A7. (a) Al(1) is coordinated by one nonbridging oxygen (O(1)) and three bridging oxygens (O(2)) with C_3 symmetry. O(1) and O(2) denote oxygens bonded to one Al and two Al ions, respectively. The direction of the electric field vector \mathbf{q} at Al(1) is parallel to the C_3 axis (i.e., $\langle 111 \rangle$ direction). (b) Al(2) is coordinated by four bridging oxygens (O(2)) with S_4 symmetry. The electric field vector \mathbf{q} at Al(2) is parallel to the S_4 axis (i.e., $\langle 100 \rangle$ direction).

e^2qQ/h in eq 7 is a nuclear quadrupole coupling constant. Muller et al. reported a value of e^2qQ/h for ^{27}Al in C12A7 by MAS-NMR measurement.²⁵ We used these reported values (Table 4) in the simulation.

By using eqs 4–17, the normalized echo intensity is obtained, and the echo decay curve as a function of T with fixed τ ($E(T)$) is expressed by eq 18

$$E(T) = \langle V_N(\tau, T) \rangle E_0 \exp\left(-\frac{T}{T_1}\right) \quad (18)$$

Here, the echo intensity without ESEEM is represented by eq 19

$$E(T) = E_0 \exp\left(-\frac{T}{T_1}\right) \quad (19)$$

$\langle V_N(\tau, T) \rangle_{\theta, \phi}$, given by eq 13, is expressed as the sum of a constant term ($0 < C < 1$) and a term vibrating around zero, $V_0(T)$

$$\langle V_N(\tau, T) \rangle_{\theta, \phi} = C + V_0(T) \quad (20)$$

By substitution of eq 20 into eq 18, we obtain the following formula

$$E(T) = [CE_0 + E_0V_0(T)] \exp\left(-\frac{T}{T_1}\right) \quad (21)$$

To extract an ESEEM pattern, an observed decay curve represented by eq 21 was fitted to the exponential decay curve $E'(T)$.

$$E'(T) = CE_0 \exp\left(-\frac{T}{T_1}\right) \quad (22)$$

With division of eq 21 by eq 22, then apparent ESEEM $V'(\tau, T)$ is obtained as

$$V'(\tau, T) = \frac{E(T)}{E'(T)} = 1 + \frac{V_0(T)}{C} \quad (23)$$

For comparison with an observed pattern $V'(\tau, T)$, the calculated ESEEM $\langle V_N(\tau, T) \rangle_{\theta, \phi}$ is normalized by a time-independent term

estimated by averaging of $\langle V_N(\tau, T) \rangle_{\theta, \phi}$ in T domain, $\langle V_N(\tau, T) \rangle_{\theta, \phi, T}$

$$V'(\tau, T) = \frac{\langle V_N(\tau, T) \rangle_{\theta, \phi}}{\langle V_N(\tau, T) \rangle_{\theta, \phi, T}} \quad (24)$$

Results and Discussion

CW-EPR of O_2^- in C12A7 Single Crystal. EPR spectra of the C12A7 single crystal exhibited several resonance lines, which are enhanced strongly after the crystal was annealed in a conventional oxygen atmosphere. The lines are attributed to $^{16}\text{O}_2^-$, and the resonance magnetic fields H_0 change continuously with a variation in the direction of the magnetic fields, H_0 , with respect to the crystal axis. Figure 3 shows angular dependence of H_0 in the CW-EPR spectra at 20 K after the thermal annealing. The magnetic field was applied parallel to the (100) plane, and it rotated from [100] axis to [110] in Figure 3a. However, the sample was rotated from $\mathbf{H} \parallel [100]$ to $\mathbf{H} \parallel [110]$ within the (110) plane in Figure 3b. The maximum numbers of resonance lines observed are seven and six in Figure 3, parts a and b, respectively. The numbers of lines are reduced when the applied magnetic field is directed parallel to specific crystallographic directions. The observed values of H_0 and corresponding concrete expressions in terms of the elements of the g tensor for $\langle 100 \rangle$, $\langle 110 \rangle$, and $\langle 111 \rangle$ are listed in Table 1. By using the g tensor obtained in Table 1 and taking crystal symmetry into

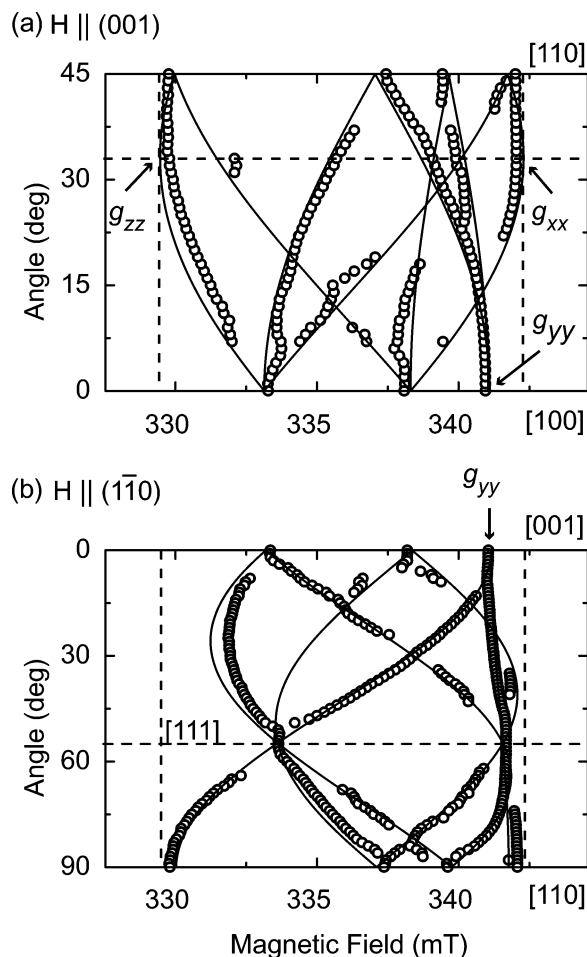


Figure 3. Angular variations for the resonance field of $^{16}\text{O}_2^-$ in C12A7 thermally treated in conventional $^{16}\text{O}_2$ gas atmosphere. The magnetic field explores the (a) (001) plane rotating from [100] to [110] and (b) in the (110) plane from [110] to [001]. The open circles denote experimental data, and the solid curves were calculated from the g tensor whose element values are shown in Table 1.

TABLE 1: EPR Parameters of O₂[−] in C12A7 Obtained from Angular Variation^a

H									
$\langle 100 \rangle$	g	$\sqrt{g_{ZZ}^2} = 2.055$		$\sqrt{g_{XX}^2} = 2.026$		$\sqrt{g_{YY}^2} = 2.009$			
	$ A^0 $ (mT)	$\sqrt{A_{ZZ}^2} = 5.1$		$\sqrt{A_{XX}^2} = 6.1$		$\sqrt{A_{YY}^2} = 1.1$			
$\langle 110 \rangle$	g	$\sqrt{\frac{g_{ZZ}^2 + g_{XX}^2}{2} + g_{ZX}^2}$ = 2.077		$\sqrt{\frac{g_{YY}^2 + g_{ZZ}^2}{2}}$ = 2.031		$\sqrt{\frac{g_{XX}^2 + g_{YY}^2}{2}}$ = 2.018		$\sqrt{\frac{g_{ZZ}^2 + g_{ZZ}^2}{2} - g_{ZX}^2}$ 2.003	
	$ A^0 $ (mT)	$\sqrt{\frac{A_{ZZ}^2 + A_{XX}^2}{2} + A_{ZX}^2}$ < 1		$\sqrt{\frac{A_{YY}^2 + A_{ZZ}^2}{2}}$ < 3.5		$\sqrt{\frac{A_{XX}^2 + A_{YY}^2}{2}}$ = 3.5		$\sqrt{\frac{A_{ZZ}^2 + A_{ZZ}^2}{2} - A_{ZX}^2}$ = 7.7	
$\langle 111 \rangle$	g	$\sqrt{\frac{g_{XX}^2 + g_{YY}^2 + g_{ZZ}^2 + 2g_{ZX}^2}{3}} = 2.054$				$\sqrt{\frac{g_{XX}^2 + g_{YY}^2 + g_{ZZ}^2 - 2g_{ZX}^2}{3}} = 2.005$			
	$ A^0 $ (mT)	$\sqrt{\frac{A_{XX}^2 + A_{YY}^2 + A_{ZZ}^2 + 2A_{ZX}^2}{3}} < 1$				$\sqrt{\frac{A_{XX}^2 + A_{YY}^2 + A_{ZZ}^2 - 2A_{ZX}^2}{3}} = 6.4$			

^a X, Y, and Z denote axes for the crystal. The number of EPR lines at $H_0 || [\bar{1}\bar{1}0]$ in Figure 3 indicates that $g_{XY} = g_{YZ} = 0$ and $A_{XY} = A_{YZ} = 0$.

account, we can calculate the angular variation of H_0 as shown by solid curves in Figure 3.

The EPR spectra became the simplest when H_0 was directed parallel to [111]. Figure 4a shows CW-EPR spectra at 20 K of O₂[−] in the C12A7 single crystal heated in a conventional O₂ gas for this orientation. There are two signals centered at $g = 2.054$ and 2.005 in the spectrum. Both signals are attributable to the O₂[−] ions occupying chemically equivalent sites, which becomes magnetically inequivalent by the application of B_0 parallel to [111]. The absence of hyperfine structure due to neighboring ions indicates the O₂[−] ions are not located sufficiently close to a magnetic nucleus (i.e., ²⁷Al). Thus, it is concluded that they are adsorbed on Ca²⁺ ions, an inference which will be confirmed later in this study.

In the EPR spectra for the C12A7 single crystal thermally treated in 40% ¹⁷O-enriched O₂ gas atmosphere, HFS due to the ¹⁷O nucleus is observed around the peak at $g = 2.005$ (Figure 4b). When two oxygen atoms in O₂[−] ion are situated at chemically equivalent sites such as the side-on configuration (Figure 5a), the spin density of each oxygen atom is equal.¹ Then (¹⁷O¹⁶O)[−] becomes equivalent to (¹⁶O¹⁷O)[−], each giving 6 lines ($2I + 1 = 6$ where I is the nuclear spin quantum number of ¹⁷O) with an equal separation of $|A| = 5.5$ mT, whereas (¹⁷O¹⁷O)[−] gives 11 lines with the same separation as that of (¹⁷O¹⁶O)[−]. On the contrary, when two oxygen atoms are nonequivalent such as “top-on” configuration, 36 split lines ($(2I + 1)^2$) should be observed (Figure 5b). The calculated HFS for the side-on configuration, inserted in Figure 5a, agrees with the observed spectrum, consistent with the oxygen atoms in the O₂[−] ion being in chemically equivalent positions adsorbed on the Ca²⁺ ion. As will be shown later, the O₂[−] ion is adsorbed on a Ca²⁺ ion on the cage wall forming the side-on configuration.

The isotopic molecule fractions were obtained from the integrated intensity of the respective signals as 15% (¹⁷O¹⁷O)[−], 50% (¹⁷O¹⁶O)[−], and 35% (¹⁶O¹⁶O)[−]. These values are in

reasonable agreement with those expected from 40% ¹⁷O-enriched O₂ gas (16%:48%:36%). This agreement provide clear evidence that O₂[−] is created by transferring an electron, most likely from a free-oxygen ion O^{2−} in the cage to an O₂ molecule introduced into C12A7 from atmosphere (O^{2−} (cage) + O₂ (atmosphere) → O[−] (cage) + O₂[−] (cage)). The angular variation of the HFS is generally very complicated because of many lines. However, by selecting certain specific directions, the HFS can be simplified, and the absolute values of the HFS coupling constants, $|A|$, are obtained as shown in Table 1. Here, the quadrupole effect was neglected for the evaluation because the quadrupole moment of the ¹⁷O nuclei is too small to provide significant influences on the CW-EPR spectra. Remembering that the isotropic hyperfine constant must be negative because of the negative magnetogyric ratio for ¹⁷O, the signs of the principal values of the A tensor are determined as in Table 1.²⁶

By the diagonalization of the g and HF tensors whose elements are given in Table 1 (each element is the square of the value obtained from Table 1), we obtained the principal values of the tensors for the O₂[−] molecular coordination (x, y, z), which is transformed from the crystal axes of coordination (X, Y, Z). Table 2 lists the direction cosines transforming between the two coordinate systems, indicating that the x and z axes are rotated from X and Z axes by 33.5° with respect to the y axis. Figure 6a shows the schematic representation for the geometry of the Ca²⁺ ion and 2p orbitals of the O₂[−] ion in the side-on configuration. The electron energy diagram of the O₂[−] ion for the configuration is illustrated in Figure 6b. The degeneracy of the highest-occupied π_g orbitals of free O₂[−] ion is removed by the interaction with surrounding ions, in the bulk or at the surface, to split them into two components with an energy separation Δ . Kanzig and Cohen derived a theoretical expression for the g tensor of O₂[−] assuming an ionic model where the nonbonding 2p electrons of the O₂[−] ion are localized in the π_g orbitals.²⁷ The validity of this model will be confirmed

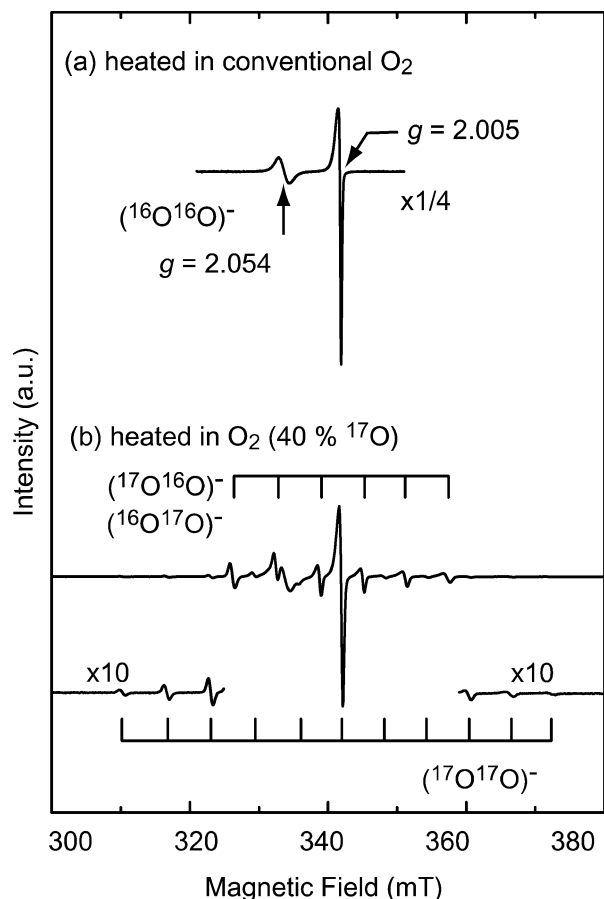


Figure 4. EPR spectrum of O_2^- in a C12A7 single crystal heated in oxygen gas with magnetic field direction parallel to the [111] direction. The measurement temperature is 20 K. (a) Spectrum for the sample heated in a conventional O_2 gas. Two signals were observed at $g = 2.054$ and 2.005 , each of which originates from crystallographically equivalent O_2^- at chiral sites with respect to [111] direction. (b) Spectrum for the sample heated in 40% ^{17}O -enriched oxygen gas. Also shown as combs are hyperfine splittings due to ^{17}O in $(^{16}\text{O}^{17}\text{O})^-$ and $(^{17}\text{O}^{17}\text{O})^-$ calculated for the side-on configuration.

by the analysis of the ^{17}O HFS tensor described later. In their model, the principal values of the g tensor are given by eqs 25–27.

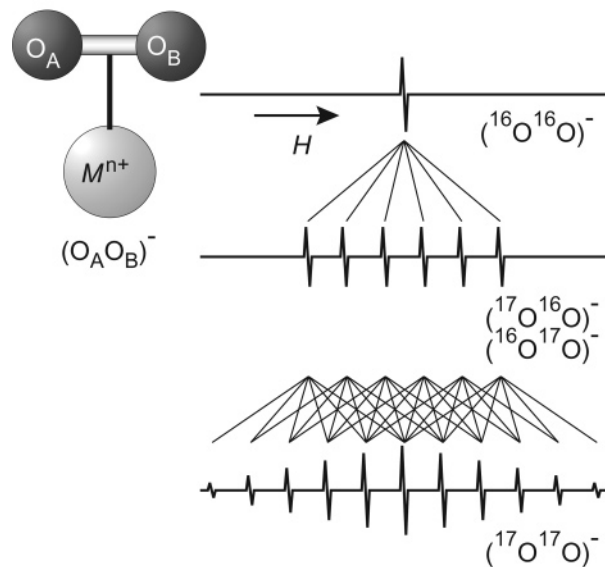
$$g_{xx} = g_e \left[\frac{\Delta^2}{\lambda^2 + \Delta^2} \right]^{1/2} - \frac{\lambda}{E} \left\{ 1 - \left[\frac{\lambda^2}{\lambda^2 + \Delta^2} \right]^{1/2} - \left[\frac{\Delta^2}{\lambda^2 + \Delta^2} \right]^{1/2} \right\} \quad (25)$$

$$g_{yy} = g_e \left[\frac{\Delta^2}{\lambda^2 + \Delta^2} \right]^{1/2} - \frac{\lambda}{E} \left\{ \left[\frac{\lambda^2}{\lambda^2 + \Delta^2} \right]^{1/2} - \left[\frac{\Delta^2}{\lambda^2 + \Delta^2} \right]^{1/2} - 1 \right\} \quad (26)$$

$$g_{zz} = g_e - 2 \left[\frac{\lambda^2}{\lambda^2 + \Delta^2} \right]^{1/2} l \quad (27)$$

Axes of x , y , and z correspond to the molecular coordinate defined in Figure 6a. That is, the x and z axes are along the π_g orbital and the O–O bond, respectively, and the y axis is parallel to the C_2 axis in C12A7, which passes through the two Ca^{2+} ions. E and Δ are the total energy separations defined in Figure

(a) "side-on" configuration



(b) "top-on" configuration

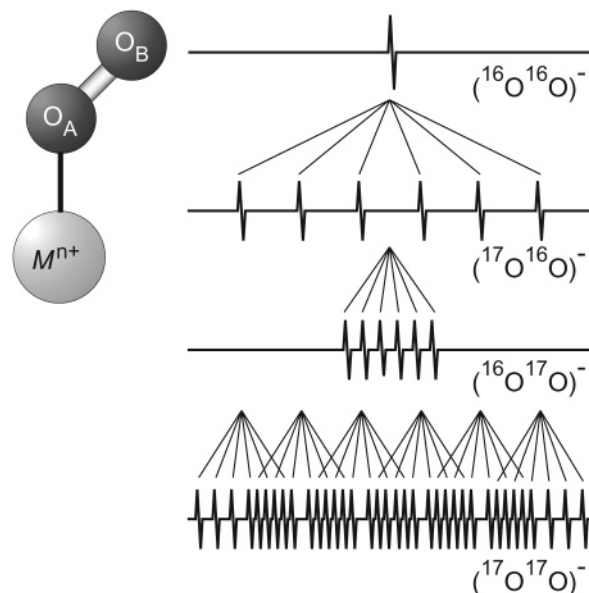


Figure 5. Two configurations for O_2^- adsorbed on a cation (M^{n+}) and schematic representation of ^{17}O hyperfine splitting for each configuration. (a) Side-on configuration having C_2 symmetry, in which two oxygen atoms are chemically equivalent and thus their spin densities are equal to each other. Then, the EPR signals of $^{17}\text{O}^{16}\text{O}^-$ and $^{16}\text{O}^{17}\text{O}^-$ are split into 6 ($=2I + 1$) lines with equal separation, and $^{17}\text{O}^{17}\text{O}^-$ is split into 11 ($=(2)2I + 1$) lines. (b) Top-on configuration. An unpaired electron is nonequivalently distributed on two oxygen atoms. Then, the EPR signals of $^{17}\text{O}^{16}\text{O}^-$ and $^{16}\text{O}^{17}\text{O}^-$ are split into 6 ($=2I + 1$) lines with a different separation interval, and $^{17}\text{O}^{17}\text{O}^-$ is split into 36 ($=(2I + 1)^2$).

6b and λ is the spin–orbital coupling constant of the O^- . The parameter l , a correction to the angular momentum about z caused by the crystal field, is usually close to 1. Thus, we assume $l = 1$ hereafter. By substitution of the observed g values in Table 2 into eqs 25–27, $\Delta = 0.43$ eV, $E = 4.6$ eV, and $\lambda = 0.017$ eV were obtained. The λ value agrees exactly with the value reported in O^- (0.0167 eV).²⁸

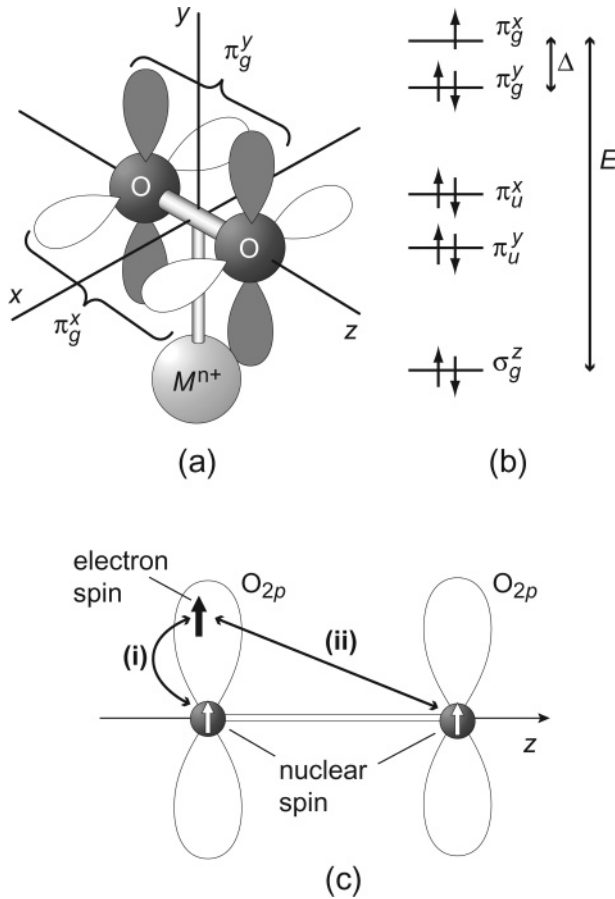


Figure 6. (a) Molecular coordinate system and (b) energy level diagram of an O₂[−] ion in the side-on configuration. The interaction of the free O₂[−] ion with the matrix removes the degeneracy of the highest occupied π_g orbitals, splitting them into two components with a separation Δ. An electron pair occupies the π_g^y level directing to the adsorption of Ca²⁺. The π_g^x orbital is occupied by an unpaired electron. (c) Two types of the dipolar interactions between an electron spin of the π_g^x electron and a nuclear spin of ¹⁷O, (i) intraatomic and (ii) interatomic.

Because of $\lambda \ll \Delta < E$, eqs 25–27 may be approximated as eq 28–30.

$$g_{xx} = g_e \quad (28)$$

$$g_{yy} = g_e + \frac{2\lambda}{E} \quad (29)$$

$$g_{zz} = g_e + \frac{2\lambda}{\Delta} \quad (30)$$

These equations indicate that the value of g_{zz} is sensitive to the kind of a cation to which the O₂[−] ion is adsorbed because Δ changes sensitively with environment. The g_{zz} value (2.080) in C12A7 is close to that (~2.09) of O₂[−] on the surface of CaO rather than that (~2.04) on Al₂O₃, providing a solid evidence that the O₂[−] ion is adsorbed on the Ca²⁺ ion forming the cage wall.¹

Next, we will estimate the spin density on the oxygen atoms from the principal values of the ¹⁷O hyperfine tensor of O₂[−] in C12A7. The energy level diagram in the side-on configuration indicates that the unpaired electron is localized mainly in the π_g^x orbital, which is composed of the 2p_x orbitals of the oxygen atoms. In this model, there are two types of dipolar interactions (Figure 6c). One is an intraatomic interaction (i) between the

TABLE 2: Principal Values of g and ¹⁷O Hyperfine Tensors for of O₂[−] in C12A7 and Directions of Principal Axes to Crystal Frame^a

		direction cosines
g_{xx}	2.002	$\langle -0.5446, 0, 0.8386 \rangle$
A_{xx}^O (mT)	−7.8	
g_{yy}	2.009	$\langle 0, 1, 0 \rangle$
A_{yy}^O (mT)	1.1	
g_{zz}	2.080	$\langle 0.8386, 0, 0.5446 \rangle$
A_{zz}^O (mT)	0.73	

^a The principal values of the g tensor are obtained by the diagonalization of the g tensor whose elements are listed in Table 1. The values of the HF tensor are also obtained under the assumption that the HF tensor has the same principal axes as the g tensor.

unpaired electron and the oxygen nucleus and the other is an interatomic interaction (ii) between the unpaired electron and the adjacent oxygen nucleus. Because the latter component is much smaller than the former, we neglected the latter term in the following discussion.

The localized electron spin induces spin polarization on the π_g^y orbital composed of the hybrid of the 2p_y and 2s orbitals, which are occupied with paired electrons. Thus, it is expected that the hyperfine tensor was represented by an isotropic term, A_{iso} , and two axial terms along the x and y axis, B_x and B_y . That is

$$\mathbf{A}^O = A_{iso} + B_x \begin{vmatrix} 2 & & \\ & -1 & \\ & & -1 \end{vmatrix} + B_y \begin{vmatrix} -1 & & \\ & 2 & \\ & & -1 \end{vmatrix} \quad (31)$$

The isotropic and the axial terms are given by

$$A_{iso} = A_0 \rho_{2s} \quad (32)$$

$$B_x = B_0 \rho_{2p}^x \quad (33)$$

$$B_y = B_0 \rho_{2p}^y \quad (34)$$

where ρ_{2s} , ρ_{2p}^x , and ρ_{2p}^y are the spin densities of the paired electron in the 2s, 2p_x, and 2p_y orbitals of the oxygen atom, and A_0 and B_0 are the hyperfine constants for free 2s and 2p oxygen orbitals.

The observed \mathbf{A}^O tensor for ¹⁷O in C12A7 in Table 2 was decomposed into three terms represented by eq 35.

$$\begin{vmatrix} -7.8 & & \\ & 1.1 & \\ & & 0.73 \end{vmatrix} = -1.99 - 2.84 \begin{vmatrix} 2 & & \\ & -1 & \\ & & -1 \end{vmatrix} + 0.12 \begin{vmatrix} -1 & & \\ & 2 & \\ & & 1 \end{vmatrix} \quad (\text{mT}) \quad (35)$$

The dipolar tensor components B along the x and y directions indicate that the spin densities are positive in the 2p_x orbital but negative in the 2p_y. The B value in a free space ($B_0 = \frac{4}{5} g^O \beta_n \langle r^{-3} \rangle_{2p}$) is −6.009 mT for ¹⁷O.²⁶ We evaluate the spin density on the oxygen 2p orbital by comparing the experimentally derived dipolar component B with that obtained from $\rho_{2p}^{x(y)} = B_{x(y)}/B_0$. The values obtained are $\rho_{2p}^x = -2.84 / -6.009 = 0.47$ and $\rho_{2p}^y = 0.12 / -6.009 = -0.019$. Similarly, the spin density on the 2s orbital (ρ_{2s}) was calculated using eq 32, $\rho_{2s} = -1.99 / -187.8 = 0.011$ for $A_0 = -187.8$ mT. Thus, the total density of the unpaired electron on the two oxygen atoms is equal to 0.92,

TABLE 3: Molecular Parameters and Spin Densities Obtained from g and ^{17}O Hyperfine Tensors

λ (eV)	Δ (eV)	E (eV)	ρ_{π}^x	ρ_{π}^y	ρ_{2s}
0.017	0.43	4.6	0.94	-0.038	0.011

which is consistent with an ionic model for O_2^- in C12A7. Table 3 summarizes spin densities obtained from the ^{17}O hyperfine tensor.

If the 2s spin density arises from a spin-polarization mechanism induced by the electron spin in the 2p orbital, then only the 2p population is needed to calculate A_{iso} . For organic and inorganic peroxy radicals, the relation, $A_{\text{iso}} = Q^0 \rho_{2p}^0$, is valid, where $Q^0 = -4.1 \pm 0.3$ mT and ρ_{2p}^0 is spin density on the 2p orbital.²⁹ For O_2^- with magnetically equivalent nuclei and a π spin density of unity, the value of $A_{\text{iso}} = -(4.1 \pm 0.3)/2 = -2.05 \pm 0.15$ mT is expected. This value agrees well with the observed value $A_{\text{iso}} = -1.99$ mT, further verifying the superoxide radical in C12A7 has pure π character.

The information obtained from CW-EPR of the single crystalline C12A7 is summarized as follows. (i) The O_2^- ion in C12A7 is adsorbed on a Ca^{2+} . (ii) The two oxygen atoms in O_2^- are chemically equivalent. (iii) The x and z axes in the O_2^- molecular coordination are rotated from the crystal coordination by $\sim 33.5^\circ$ about the y axis.

Each cage in C12A7 is crystallographically equivalent (having S_4 symmetry) if it is not occupied by an anion. It also has a 2-fold rotational axis (C_2) through the center, on which two of six Ca^{2+} ions are located. Thus, the cages are classified into three types depending on the direction of the C_2 axis, parallel to X ([100]), Y ([010]), or Z axis ([001]). The result (ii) requires that the C_2 axis is perpendicular to O–O bond and passes through the middle point of the bond.

Provided that the O_2^- ion is encaged, directly shown by the pulsed EPR measurement later, the information derived from CW-EPR leads to two possible structures for the O_2^- ion shown in Figure 7. In both configurations, the interaction between paired electrons in the π_g^y orbital and Ca^{2+} ions on the C_2 axis forces the y axis to align parallel to C_2 axis. In configuration a, the x axis rotates from the X axis by 33.5° , whereas the z axis rotates from the X axis by the same angle in configuration b. Although it is clarified that the O_2^- ion is adsorbed on Ca^{2+} , an analysis of CW-EPR spectra provides no direct information about the distance between O_2^- and Ca^{2+} ($d_{\text{O}_2-\text{Ca}}$). When O_2^- is located at the center of the cage ($d_{\text{O}_2-\text{Ca}} = 0.28$ nm), configurations a and b are equivalent, having the same stabilized energy due to the S_4 symmetry of the center. However, when O_2^- is shifted from the cage center toward one of the Ca^{2+} ions on the C_2 axis, the stabilized energy becomes different due to the fact that the interaction between the π_g^x electron and 4 Ca^{2+} ions is attractive and the interaction with O_2^- ions on the wall is repulsive. On the basis of the geometrical structure of the π_g orbital, the configuration of Figure 7a, where the π_g^x orbital points toward the Ca^{2+} ions, is energetically more favorable compared to configuration b whose π_g^x orbital points toward the O_2^- ions.

Analysis of ESEEM on C12A7. Figure 8, parts a and c, respectively, shows two-pulsed and three-pulsed echo decay curves of O_2^- in polycrystalline C12A7 at 4 K. Each spectrum consists of ESEEM superposed on an exponential decayed curve. Parts b and d of Figure 8 are frequency domain spectra of the ESEEM components, so-called FT-ESEEM spectra, obtained by Fourier transformation of corresponding ESEEM. In the FT-ESEEM spectra, there is a frequency band centered at 3.8 MHz, which agrees with the NMR frequency (ν_n) of ^{27}Al at $H_0 =$

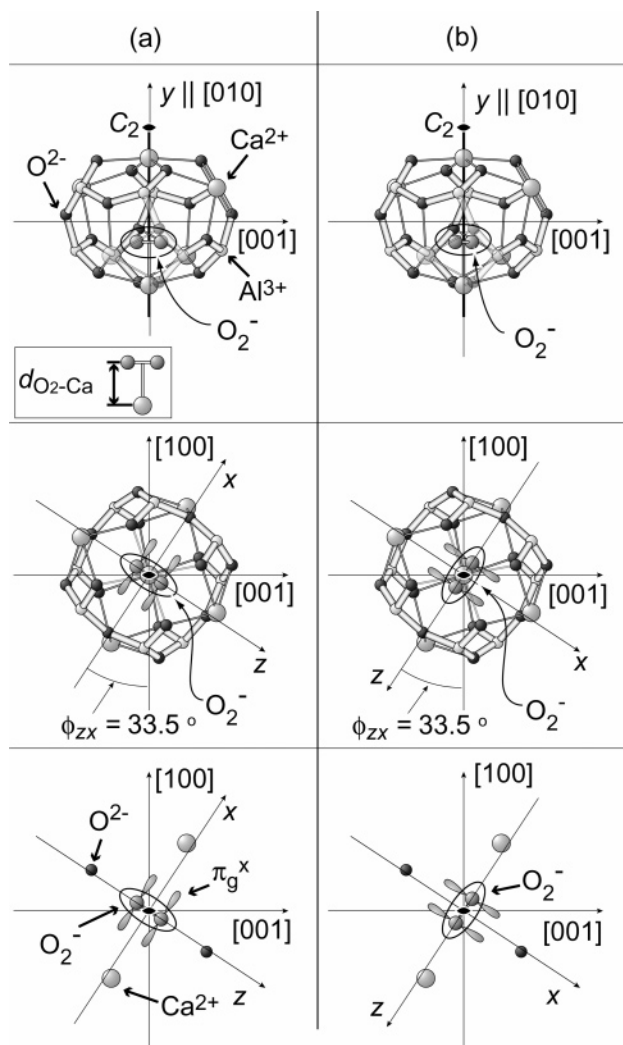


Figure 7. Two possible side-on configurations (a and b) of O_2^- within a cage of C12A7. The top and middle show top view and side view, respectively. The bottom shows the orientation of the π_g^x orbital, which is semioccupied and directs toward the neighboring Ca^{2+} on the cage wall in model a. However, the π_g^x orbital directs toward the O_2^- on the cage wall in configuration b. Each cage of C12A7 has C_2 symmetry, and the cage wall consists of 6 Ca^{2+} , 8 Al^{3+} , and 16 O_2^- ions. O_2^- is adsorbed on either of two Ca^{2+} ions located on the C_2 axis across the center of the cage. Then, the C_2 axis is perpendicular to the interatomic bond of O_2^- and passes through the center of the bond. The interatomic bond of model a is perpendicular to that of model b. Attractive interaction between the unpaired electron in π_g^x with the second neighboring Ca^{2+} ion makes model a more favorable than model b.

340 mT, indicating that the ESEEM is induced by ^{27}Al nuclei interacting with O_2^- at a distance 0.3–0.8 nm.

Closed circles in Figure 9, parts a and b, show apparent three-pulsed ESEEM patterns $V''(\tau, T)$ of O_2^- in C12A7 extracted from an echo decay curve in Figure 8c by using eq 23. The solid curve in Figure 9a is an ESEEM pattern calculated for the structure models illustrated in Figure 7, where O_2^- is located at the middle point between two Ca^{2+} ions on the C_2 axis. An unpaired electron was assumed to be positioned at the middle point of O–O bond of O_2^- . Then, the distance ($d_{\text{O}_2-\text{Ca}}$) between the O_2^- ion and Ca^{2+} is 0.283 nm, and O_2^- is surrounded by eight neighboring Al^{3+} ions (4×0.347 nm and 4×0.367 nm). In the ESEEM simulation, the hyperfine interactions with all

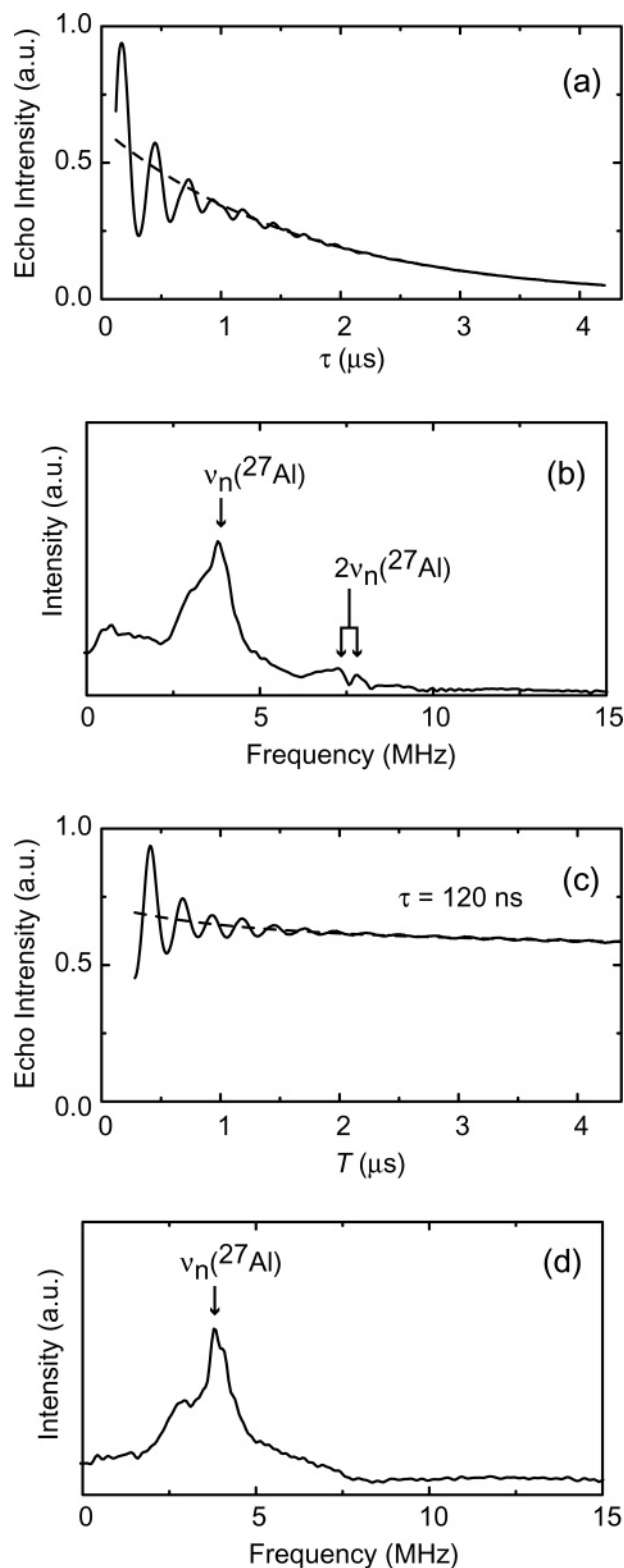


Figure 8. Pulsed-EPR spectra of O_2^- in C12A7. (a) Two-pulsed echo decay curve. (b) Frequency domain spectrum of two-pulsed ESEEM obtained by Fourier transformation of modulated component in the two-pulsed echo decay. (c) Three-pulsed echo decay curve. (d) Frequency domain spectrum of three-pulsed ESEEM. Echo decay curves and frequency domain spectra were obtained by two-pulsed and three-pulsed measurements at 4 K. Three-pulsed decay was measured with $\tau = 120$ ns. There is a primary frequency band at 3.8 MHz that agrees with the NMR frequency (ν_n) of ^{27}Al at $H_0 = 340$ mT. In addition to this band, there is another band centered at $2\nu_n$ in the two-pulsed FT-ESEEM spectrum. The $2\nu_n$ band is further split by nuclear quadrupole interaction of the nucleus with $I > 1$.

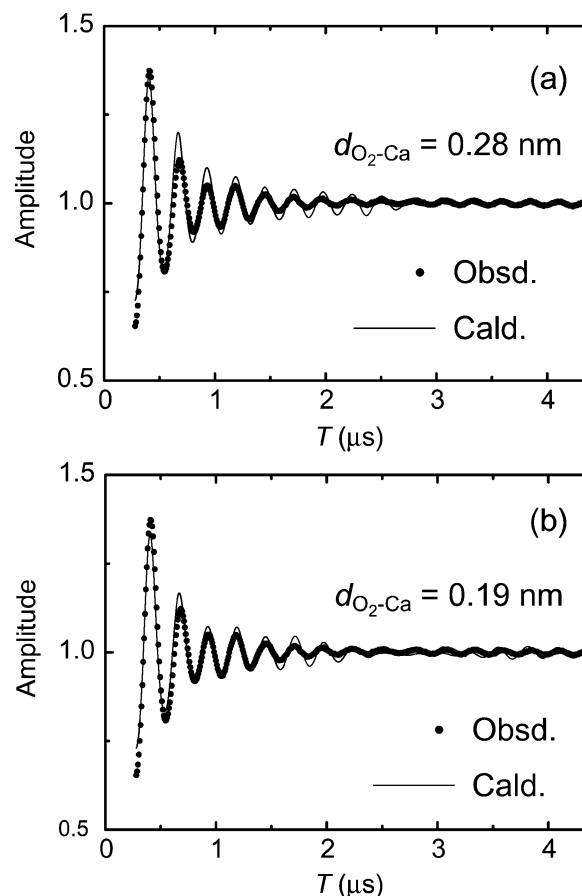


Figure 9. ESEEM pattern observed at 4 K (closed circles) and patterns calculated (solid lines) for the structural model in Figure 7 for two values of $d_{\text{O}_2-\text{Ca}}$. ESEEM patterns were calculated for (a) $d_{\text{O}_2-\text{Ca}} = 0.28$ nm and (b) $d_{\text{O}_2-\text{Ca}} = 0.19$ nm. The error of the fitting is quantified by the mean square of the residuals for all points (σ^2). The values of σ calculated for the patterns a and b are 0.023 and 0.020, respectively. Better agreement between the observed and calculated patterns is obtained for b.

TABLE 4: Atomic Position and Nuclear Parameters in C12A7

atom	site	X	Y	Z	n^a	I	ν_n^b (MHz)	e^2qQ/h^c (MHz)
Ca(1)	24d	0	$1/4$	0.1397	1	0		
Al(1)	16c	0.0187	0.0187	0.0187	1	$5/2$	3.886	11.0
Al(2)	12a	$-1/8$	0	$1/4$	1	$5/2$	3.886	3.7
O(1)	48e	0.151	-0.037	0.057	1	0		
O(2)	16c	-0.064	-0.064	-0.064	1	0		
O(3)	24d	0.3370	0	$1/4$	$1/6$	0		
cage	12b	$3/8$	0	$1/4$				

^a Site occupancy. ^b NMR frequency at 350 mT. ^c Nuclear quadrupole coupling constant.²⁵

of the Al nuclei within 0.8 nm radius are counted, and their positions were calculated by using atomic coordinates specified in Table 4.

The maximum amplitude of the calculated ESEEM pattern is almost the same as that of the observed ESEEM pattern. However, the decay rate of the amplitude in T domain is slower than that of observed one. In the ESEEM simulation, the decay rate strongly reflects the distance of the O_2^- and the nearest Al^{3+} nuclei. To obtain an improved fitting by the fast decaying of modulation, the position of O_2^- was shifted toward one of the nearest Ca^{2+} ions along the center axis. Consequently, the distance between O_2^- and the nearest Al^{3+} was also decreased. When $d_{\text{O}_2-\text{Ca}}$ became 0.19 nm, the best fitting shown in Figure

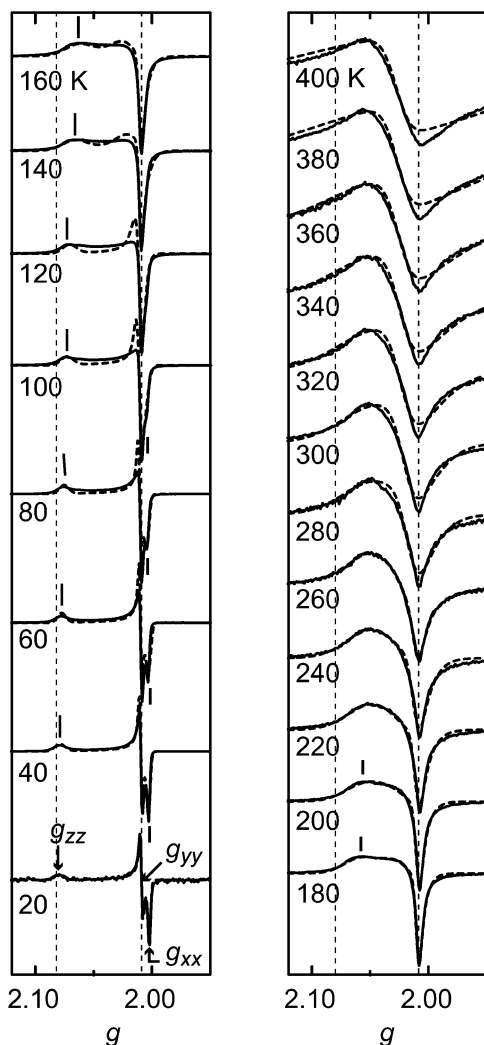


Figure 10. Variation in EPR line shape of O_2^- in polycrystalline C12A7 with temperature (—, observed; ---, simulated).

9b was attained (the distances to the neighboring Al nuclei are 2×0.325 nm, 2×0.340 nm, 2×0.389 nm, and 2×0.412 nm). The distance $d_{\text{O}_2-\text{Ca}} = 0.19$ nm is close to that in the alkali superoxide (~ 0.21 nm in NaO_2).^{30,31} Therefore, the ESEEM simulation revealed that the observed ESEEM pattern is consistent with the clathrate structure of O_2^- shown in Figure 7a with $d_{\text{O}_2-\text{Ca}} = 0.19$ nm.

Temperature Variation of g Tensor and Dynamics of O_2^- . Figure 10 shows CW-EPR spectra of O_2^- in C12A7 powder measurement at various temperatures from 20 to 400 K. Below 80 K, an EPR spectrum is asymmetric in shape, corresponding to an orthorhombic g tensor. Thus, we can directly determine the principal values of the g tensor, g'_{xx} , g'_{yy} , and g'_{zz} , from singular spectral features ($g'_{zz} > g'_{yy} > g'_{xx}$). With an increase in temperature, a decrease in g'_{zz} and an increase in g'_{xx} are observed, although g'_{yy} remains almost constant. At ~ 100 K, g'_{xx} becomes equal to g'_{yy} , and the line shape appears to possess an axial symmetry ($g'_{zz} > g'_{yy} = g'_{xx}$). Above ~ 120 K, the g'_{xx} and g'_{yy} values cannot be evaluated directly from the observed spectra, although g'_{zz} can be evaluated.

Therefore, we performed a powder pattern fitting to evaluate all of the g values. In the fitting, a powder pattern was simulated by assuming random orientation of an O_2^- with respect to the applied magnetic field. The line shape of each spectrum was calculated using a pseudo-Voigt function as the convolution

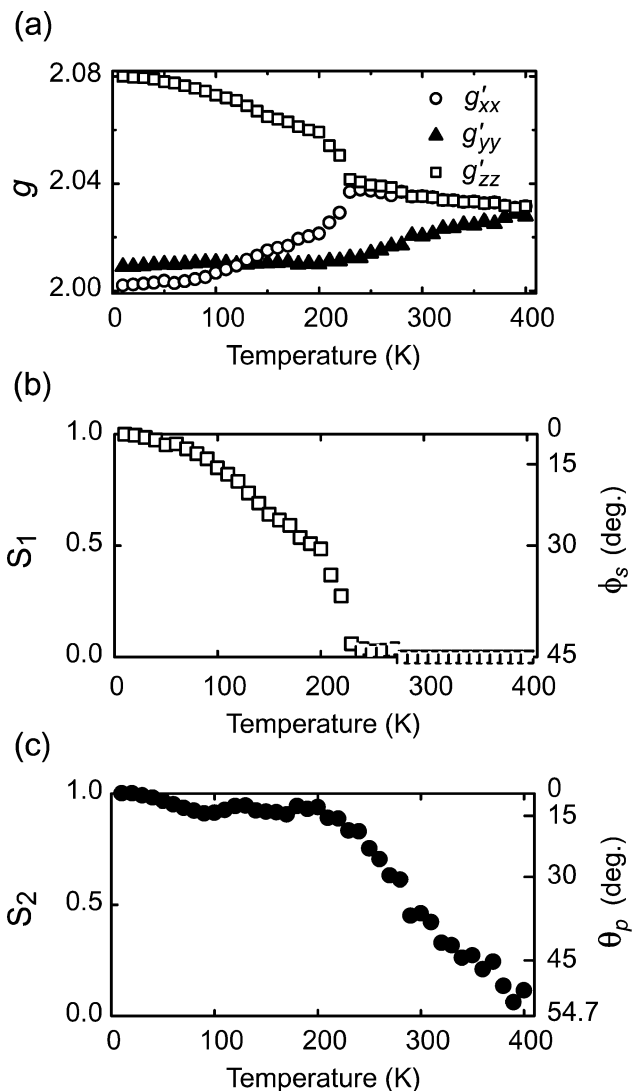


Figure 11. Temperature variation of the principal g values and order parameters of O_2^- in C12A7. (a) The principal g values (g'_{xx} , g'_{yy} , and g'_{zz}) obtained through spectral fitting shown in Figure 10. (b) Order parameter S_1 showing mean rocking angle (ϕ_s) of the x and z axes of O_2^- about C_2 axis of the cage. (c) Order parameter S_2 showing the mean precession angle (θ_p) of the y axis of O_2^- about the center axis of the cage.

function, which is centered at the resonance fields calculated by the principal values of the g tensor and has a line width calculated according to the tensor having the common principal axes with the g tensor.³² The amplitude, g tensor, line width, and Gaussian–Lorentzian ratio were optimized by the SIMPLEX method.^{33,34} Above 260 K, the powder patterns were simulated by employing an axial g tensor ($g'_{||} = g'_{xx}$, $g'_{\perp} = g'_{xx} = g'_{zz}$). Figure 11a shows g values obtained by the fitting as a function of temperature.

Below 220 K, g'_{zz} decreases and g'_{xx} increases with temperature whereas g'_{yy} and the averaged g value, $\bar{g} = \sqrt{(g'^2_{xx} + g'^2_{yy} + g'^2_{zz})/3}$, remains almost constant ($g'_{xx} \cong 2.01$ and $\bar{g} \cong 2.03$). This variation is explained by a rocking motion of O_2^- about the y axis like a seesaw (Figure 12a). The direction of the interatomic bond in O_2^- changes while magnetic resonance phenomenon occurs. This motion admixes g_{xx} and g_{zz} with each other. Then, the apparent g values, g'_{xx} and g'_{zz} , may be expressed by using mean square cosine of rocking angle ϕ_s ($0 < \langle \cos^2 \phi_s \rangle < 1/2$) and the g values ($g_{xx} = 2.002$, $g_{yy} =$

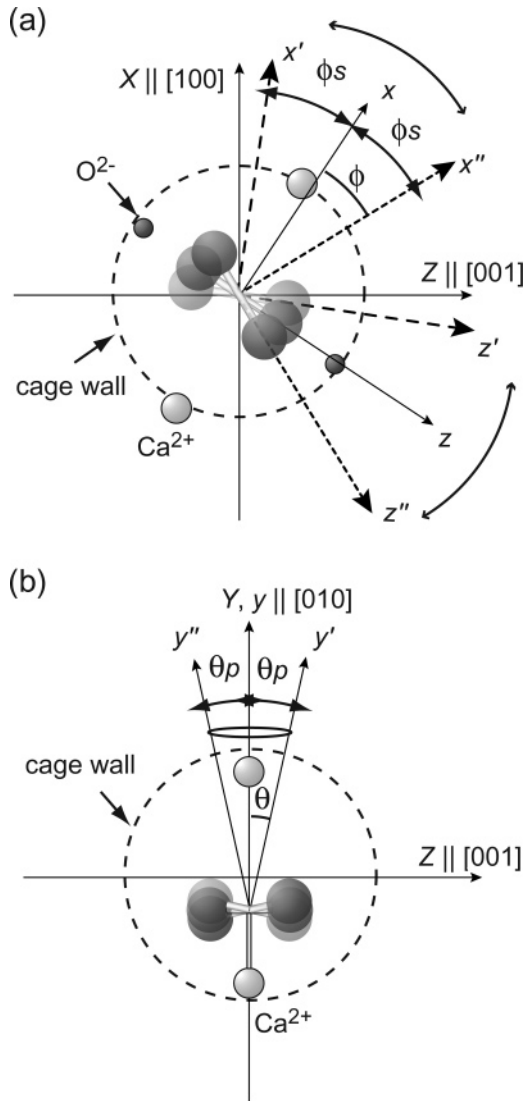


Figure 12. Motional modes of O₂⁻ in the cage of C12A7. (a) The rocking motion of the interatomic bond of O₂⁻ about the center axis of cage. ϕ indicates an angle between the direction of the interatomic bond (z' or z'') and the mean z direction determined by the EPR measurements on the single crystal. ϕ oscillates between $-\phi_s$ and ϕ_s while magnetic resonance phenomenon occurs. (b) The precession motion of the y axis of O₂⁻ about the C_2 axis in the cage. θ indicates an angle between the y axis and the center axis of the cage.

2.009, and $g_{zz} = 2.080$) for the solidlike O₂⁻ observed below 20 K.

$$g_{xx}'^2 = g_{xx}^2 \langle \cos^2 \phi_s \rangle + g_{zz}^2 \langle \sin^2 \phi_s \rangle \quad (36)$$

$$g_{zz}'^2 = g_{xx}^2 \langle \sin^2 \phi_s \rangle + g_{zz}^2 \langle \cos^2 \phi_s \rangle \quad (37)$$

Here, we introduce an order parameter S_1 ($0 < S_1 < 1$) defined by eq 38.

$$S_1 = 2 \langle \cos^2 \phi_s \rangle - 1 = \frac{g_{zz}'^2 - g_{xx}'^2}{g_{zz}^2 - g_{xx}^2} \quad (38)$$

Open squares in Figure 11b represent the temperature variation of S_1 and ϕ_s . The ϕ_s value increases with temperature and becomes larger than 45° above 220 K. Then, the g tensor appears to possess an axial symmetry, whereas the y axis is almost fixed.

Above 220 K, both $g_{||}$ and g_{\perp} converge gradually to $\bar{g} \approx 2.03$. This behavior is explained by the precession of the y axis about the crystal Y axis (Figure 12b) (i.e., $g_{||}'$ and g_{\perp}' may be expressed by a mean tilting angle θ_p ($0 < \theta_p < \cos(1/3)^{1/2} \approx 54.7^\circ$), $g_{||} = g_{xx}$ and $g_{\perp} = (g_{xx}^2 + g_{zz}^2)/2$

$$g_{||}'^2 = g_{||}^2 \langle \cos^2 \theta_p \rangle + 2g_{\perp}^2 \langle \sin^2 \theta_p \rangle \quad (39)$$

$$g_{\perp}'^2 = 2g_{||}^2 \langle \sin^2 \theta_p \rangle + g_{\perp}^2 \langle \cos^2 \theta_p \rangle \quad (40)$$

By use of these equations, the parameter S_2 ($0 < S_2 < 1$) is defined by eq 41.

$$S_2 = \frac{3 \langle \cos^2 \theta_p \rangle - 1}{2} = \frac{g_{||}'^2 - g_{\perp}'^2}{g_{||}^2 - g_{\perp}^2} \quad (41)$$

To calculate S_2 below 270 K, g_{\perp}^2 is substituted by $(g_{zz}'^2 + g_{xx}'^2)/2$. Solid circles in Figure 11c show the temperature variation of S_2 and θ_p . Below ~ 220 K, the y axis of O₂⁻ is aligned with the center axis of the cage (Y axis in Figure 12) and θ_p is suppressed below $\sim 10^\circ$. Above ~ 220 K, θ_p increases with temperature. However, even at 400 K, the line shape is still asymmetric ($g_{||} \neq g_{\perp}$) (i.e., the motion with tilting of the y axis is restrained even at high temperatures). This observation means that θ_p increases but does not reach the value of 54.7° corresponding to free rotation of O₂⁻ within temperature range examined here.

In the clathrate model (Figure 7) of O₂⁻ in C12A7, the π_g^y paired electrons of the O₂⁻ strongly interact with the first neighboring Ca²⁺. This model suggests that the y axis of the O₂⁻ is fixed to be parallel to the C_2 axis of the cage. This is consistent with an experimental result that the motion altering the direction of the y axis is suppressed at even high temperature. Similarly, the interaction between the π_g^x unpaired electron and the second neighboring Ca²⁺ ions is expected to fix the x and z axis. However, the experimental results indicate that this effect is relatively small, and the motion, which alters the directions of the x and z axis but retains the y axis, is thermally activated at even low temperature.

In the previous studies, the EPR spectra of paramagnetic centers affected by molecular motion were simulated using density matrix formalism based on the stochastic Liouville equation with several motional models including Brownian rotational diffusion, non-Brownian rotational diffusion, anisotropic viscosity, and discrete jump.^{35,36} However, we could not reproduce the EPR line shape of O₂⁻ in C12A7 by using this method. It is likely that the motion of O₂⁻ in C12A7 is so complicated by a mixture of several types of motions that the line shape cannot be explained by a simple motional model.

Conclusions

By using ¹⁷O enrichment technique, we observed ¹⁷O EPR hyperfine splitting of O₂⁻ in C12A7. The analyses of the g and ¹⁷O hyperfine tensors obtained from the CW-EPR spectra of the single crystal reveal that the clathrate structure of O₂⁻ in the cage of C12A7 has C_2 symmetry, which is similar to that in alkali metal superoxides or superoxides in alkali halides.^{27,37} In this clathrate structure, an O₂⁻ is adsorbed on a Ca²⁺ ion in a side-on configuration with the fully occupied molecular orbital (π_g^y) directed to the Ca²⁺ ion. Comparison of the observed three-pulsed ESEEM powder pattern with simulated patterns for structural models led to the conclusion that O₂⁻ is encaged taking the side-on configuration on the Ca²⁺ forming the cage

wall. The temperature variation in the line shape of the powder EPR spectra indicates that the rocking motion of the interatomic bond about y axis parallel to the C_2 axis of the cage is thermally activated above 20 K although the motion with variation of the y direction is suppressed at even high temperature (~ 400 K). O_2^- is stabilized as a consequence of strong interaction with Ca^{2+} ions in the wall of the cage. This situation is similar to an anion vacancy in an alkali halide that traps O_2^- , O^- , H^- , e^- , and other unstable anions.^{37–40}

Acknowledgment. This work was supported by a Grant-in-Aid for Creative Scientific Research (No. 16GS01205) from the Japanese Ministry of Education, Science, and Culture.

References and Notes

- (1) Che, M.; Tench, A. J. *Adv. Catal.* **1983**, *32*, 1–148.
- (2) Chiesa, M.; Giamello, E.; Paganini, M. C.; Sojkaa, Z.; Murphy, D. M. *J. Chem. Phys.* **2002**, *116*, 4266–4274.
- (3) Lunsford, J. H. *Adv. Catal.* **1972**, *22*, 265–344.
- (4) Hosono, H.; Abe, Y. *Inorg. Chem.* **1987**, *26*, 1192–1195.
- (5) Hayashi, K.; Matsuishi, S.; Hirano, M.; Hosono, H. *J. Am. Chem. Soc.* **2002**, *124*, 738–739.
- (6) K. Hayashi, S. Matsuishi, N. Ueda, M. Hirano, H. Hosono, *Chem. Mater.* **2003**, *15*, 1851–1854.
- (7) Bartl, H.; Scheller, T. *Neues Jahrb. Mineral., Monatsh.* **1970**, *35*, 547–552.
- (8) Imlach, J. A.; Glasser, L. S. D.; Glasser, F. P. *Cem. Concr. Res.* **1971**, *1*, 57–61.
- (9) Jeevaratnam, J.; Glasser, F. P.; Glasser, L. S. D. *J. Am. Ceram. Soc.* **1964**, *47*, 105–106.
- (10) Hayashi, K.; Matsuishi, S.; Kamiya, T.; Hirano, M.; Hosono, H. *Nature* **2002**, *419*, 462–465.
- (11) Sushko, P. V.; Schluger, A. L.; Hayashi, K.; Hirano, M.; Hosono, H. *Thin Solid Films* **2003**, *445*, 161–167.
- (12) Miyakawa, M.; Hayashi, K.; Hirano, M.; Toda, Y.; Kamiya, T.; Hosono, H. *Adv. Mater.* **2003**, *15*, 1100–1103.
- (13) Matsuishi, S.; Toda, Y.; Miyakawa, M.; Hayashi, K.; Hirano, M.; Tanaka, I.; Hosono, H. *Science* **2003**, *301*, 626–629.
- (14) P. V. Sushko, A. L. Schluger, K. Hayashi, M. Hirano, H. Hosono, *Phys. Rev. Lett.* **2003**, *91*, 126401.
- (15) Li, Q.-X.; Hayashi, K.; Nishioka, M.; Kashiwagi, H.; Hirano, M.; Hosono, H.; Sadakata, M. *Appl. Phys. Lett.* **2002**, *80*, 4259–4261.
- (16) Hayashi, K.; Hirano, M.; Li, Q.-X.; Nishioka, M.; Sadakata, M.; Torimoto, Y.; Matsuishi, S.; Hosono, H. *Electrochem. Solid-State Lett.* **2002**, *5*, J13–J16.
- (17) Toda, Y.; Matsuishi, S.; Hayashi, K.; Ueda, K.; Kamiya, T.; Hirano, M.; Hosono, H. *Adv. Mater.* **2004**, *16*, 685–689.
- (18) Rowan, L. G.; Hahn, E. L.; Mims, W. B. *Phys. Rev.* **1965**, *137*, A61–A71.
- (19) Mims, W. B. *Phys. Rev. B: Condens. Matter. Matter Phys.* **1972**, *5*, 2409–2419.
- (20) Dikanov, S. A.; Tsvetkov, Y. D. *Electron Spin–Echo Envelope Modulation (ESEEM) Spectroscopy*; CRC Press: Boston, 1992.
- (21) Watauchi, S.; Tanaka, I.; Hayashi, K.; Hirano, M.; Hosono, H. *J. Cryst. Growth* **2002**, *237–239*, 801–805.
- (22) Hahn, E. L. *Phys. Rev.* **1950**, *80*, 580–594.
- (23) Dikanov, S. A.; Shubin, A. A.; Parmon, V. N. *J. Magn. Reson.* **1981**, *42*, 474–487.
- (24) Shubin, A. A.; Dikanov, S. A. *J. Magn. Reson.* **1983**, *52*, 1–12.
- (25) Muller, D.; Gessener, W.; Samoson, A.; Lippmaa, E.; Scheller, G. *Polyhedron* **1986**, *5*, 779–785.
- (26) Weil, J. A.; Bolton, J. R.; Wertz, J. E. *Electron Paramagnetic Resonance: Elementary Theory and Practical Applications*; John Wiley & Sons: New York, 1994.
- (27) Kanizig, W.; Cohen, M. H. *Phys. Rev. Lett.* **1959**, *3*, 509–510.
- (28) Bartram, R. H.; Swenberg, C. E.; Fournier, J. T. *Phys. Rev.* **1965**, *139*, A941–A945.
- (29) Melamud, E.; Silver, B. L. *J. Phys. Chem.* **1973**, *77*, 1896–1899.
- (30) Ziegler, M.; Rosenfeld, M.; Kaenzig, W.; Fischer, P. *Helv. Phys. Acta* **1976**, *49*, 57–90.
- (31) Lindsay, D. M.; Herschbach, D. R.; Kwiram, A. L. *Chem. Phys. Lett.* **1974**, *25*, 175–181.
- (32) Pilbrow, J. R. *J. Magn. Reson.* **1984**, *58*, 186–213.
- (33) Spendly, W.; Hext, G. R.; Himsworth, F. R. *Technometrics* **1962**, *4*, 441–451.
- (34) Nelder, J. A.; Mead, R. *Computer J.* **1965**, *7*, 308–313.
- (35) Shiotani, M.; Moro, G.; Freed, J. H. *J. Chem. Phys.* **1981**, *74*, 2616–2640.
- (36) Budil, D. E.; Lee, S.; Saxena, S.; Freed, J. H. *J. Magn. Reson.* **1996**, *A120*, 155–189.
- (37) Zeller, H. R.; Kanizig, W. *Helv. Phys. Acta* **1967**, *40*, 845–874.
- (38) Brailsford, J. R.; Morton, J. R. *J. Chem. Phys.* **1969**, *51*, 4794–4798.
- (39) Seitz, F. *Rev. Mod. Phys.* **1946**, *18*, 384–408.
- (40) Seitz, F. *Rev. Mod. Phys.* **1954**, *26*, 7–94.